High-fidelity and rapid cellular-level Mueller matrix imaging for tissue identification with unstained sections

JIAZHI WANG,[1] YANQIU LI,[1,2,*] CHENLE CAO,[1] GUODONG ZHOU,[1] AND LI LI[1,3]

[1]*Key Laboratory of Photoelectronic Imaging Technology and System of Ministry of Education of China, School of Optics and Photonics, Beijing Institute of Technology, 5 South Zhongguancun Street, Beijing 100081, China*

[2]*Institute of Engineering Medicine, Beijing Institute of Technology, 5 South Zhongguancun Street, Beijing 100081, China*

[3]*Chinese People's Liberation Army General Hospital, The 8th Medical Center, 17 South Heishanhu Street, Beijing 100091, China*

[*]*liyanqiu@bit.edu.cn*

Abstract: Mueller matrix polarimetry is regarded as a promising technique in the field of biomedicine, especially for pathological diagnosis. However, the current studies on Mueller imaging of pathological sections are all at the tissue-level, and the cellular-level polarization information is difficult to obtain. To overcome this challenge, we first propose a cellular-level Mueller matrix imaging method for accurate quantitative identification of tissues in this study. Benefiting from the significant birefringent behavior of paraffin in unstained sections, the proposed method can locate the paraffin distribution areas of retardance images by involving Otsu's algorithm. Then, the real cellular-level polarization information (e.g., depolarization) is acquired. The efficiency of the proposed method was demonstrated on unstained rat tissue samples. The results showed that the obtained depolarization images are highly consistent with the stained microscopic images in terms of the morphology and arrangement of the tissues at cellular level. Finally, this method was preliminarily applied to the detection of human lung cancer tissue section, effectively realizing the quantitative differentiation of normal, inflamed, and malignant areas in unstained section. This study provides a possible approach for the rapid and accurate diagnosis of cancer.

1.   Introduction

Histopathological observation is currently regarded as the "gold standard" for cancer diagnosis [1–4]. In this approach, the tissue section is observed through a high-resolution optical microscope. The morphology and arrangement of the cells are analyzed for the presence of malignancy by pathologists [5,6]. However, in this process, the section requires being stained, which is indispensable and time consuming. If the quality of the section staining is unsatisfactory, the biopsy results can be affected [7,8]. Moreover, histopathological pathological observation is difficult to provide quantitative diagnostic indicators.

Polarization imaging techniques are sensitive to microstructural changes in tissues, and can therefore be regarded as potential and label-free tools for physiological process monitoring and pathological diagnosis [9–12]. Among the current polarization imaging techniques, Mueller matrix imaging (MMI) can quantitatively provide complete polarization information of tissue samples [13–15]. Through Mueller matrix decomposition, the polarization parameters that are closely related to the microstructure variations of the samples can be obtained [16–21]. For biological tissue samples, MMI can characterize changes in the tissue microstructure using different Mueller matrix derived parameters. It has thus been applied to the detection of various

cancers, such as cervical cancer [22–25], breast ductal cancer [26–27], skin cancer [28–30], and liver cancer [31,32]. Current studies of MMI in cancer diagnosis using pathological tissue slices primarily focus on obtaining the tissue-level information of fiber changes with a low magnification objective. By analyzing the retardance-related Mueller matrix derived parameters, the density and arrangement of fibers on the slice are determined to discriminate and stage the cancer. There are also some studies focusing on exploring the influence of section conditions or imaging methods changing on polarization measurement [33,34]. These studies provide a basis for the selection and measurement of pathological sections in the future. However, even though the conventional Mueller matrix measurement for unstained slices was performed with a higher magnification objective, such arrangement is difficult to obtain the real cellular-level polarization information of tissue and identifying the exact cell structure, due to chemical immersion (e.g. paraffin or xylene immersion) during slice preparation process and the polarization aberration caused by the high NA objective. The calibration of high NA system has been completed in our previous work [35,36]. This study focuses on eliminating the effect of paraffin immersion on polarization imaging for unstained sections.

In this paper, a method of cellular-level Mueller matrix imaging for unstained sections is proposed. To the best of our knowledge, this proposal is the first of its kind. The proposed method leverages the significant birefringent behavior of paraffin in unstained sections. It identifies the paraffin distribution areas of retardance images by using Otsu's algorithm [37]. The proposed method thereby acquires the real polarization characteristics of the cellular-level microstructures in the slice. In this study, the presented technique was illustrated by measuring different tissue samples of rat. Quantitative measurements showed that without staining, the depolarization images obtained by the proposed method are highly consistent with the stained microscopic images in terms of the morphology and arrangement of the tissues at cellular level, which can realize accurate tissue identification. Finally, we preliminarily applied this technique to the detection of unstained human lung cancer section. The results indicate that the depolarization images can accurate identification of the normal, inflamed, and malignant regions in the section. Further analysis of the polarization characteristics revealed that the proposed method provided abundant information on the internal cell structure which shows great potential for the rapid and accurate diagnosis of cancer in the future.

2. Methods and materials

2.1. Experimental setup

The Mueller matrix polarimeter employed in this study was mainly composed of a light source module (a LED and filter), an illumination and imaging module (condenser and objective lens), a polarization modulator module consisting of a polarization state generator (PSG) and a polarization state analyzer (PSA), and an image detection module (spectrometer camera), as shown in Fig. 1. The light emitted from the LED (Thorlabs Solis -3C) passed through the filter (F1, Thorlabs FB650-10) with a central wavelength of 650 nm (±10 nm). Subsequently, this monochromatic light was directed to the PSG that consists of a polarizer (P1, Newport 10LP-VIS-B) and a quarter-wave plate (R1, Newport 10RP54-1B) for polarization modulation. The modulated polarized light was then focused on the sample surface by the condenser (C1, Nikon MBL11300), and the outgoing light carried the sample polarization information. The light was then collected by the objective lens (Nikon MUE61900). Next, the polarization state of the light was analyzed by the PSA, which consisted of a quarter-wave plate (R2, Newport 10RP54-1B) and a polarizer (P2, Newport 10LP-VIS-B). Finally, a reflector was employed to reflect the light onto a detector (Andor Zyla 4.2 Plus) for imaging. In this paper, we adopted complete Mueller polarimetry instead of simple orthogonal state contrast microscopy. This is because we need to obtain not only the depolarization characteristics but also the retardance

characteristics of the slices. More other polarization characteristics of the samples such as diattenuation and orientation angle will also be studied in the future.
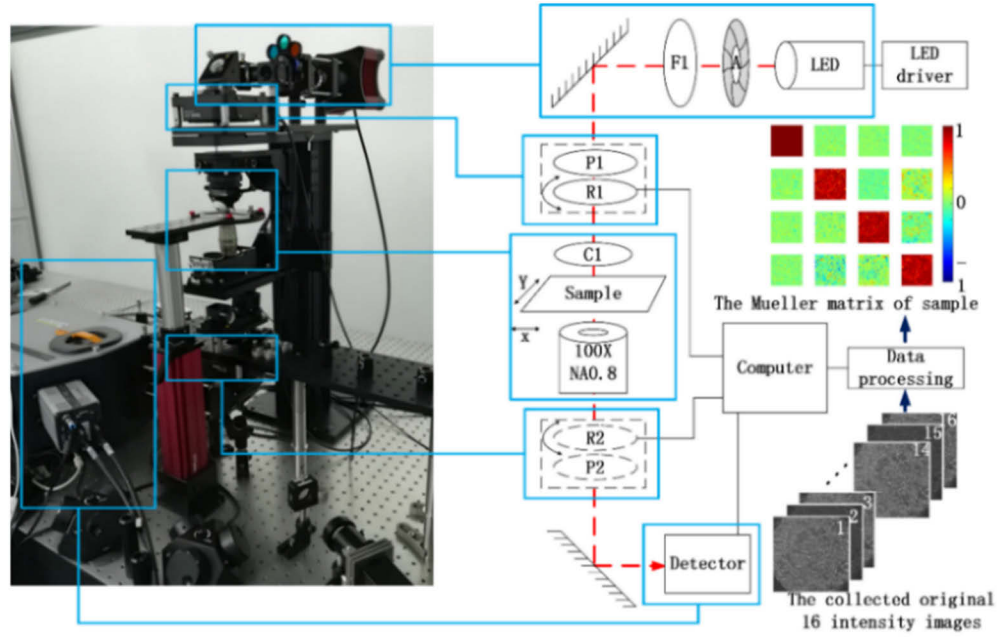
Fig. 1. Photograph of the Mueller matrix microscope.

In our experiment, the Mueller matrix of the sample was measured using the dual-rotating-retarder polarimeter (DRRP). The system calibration was performed before the measurement of tissue. We use multi-step eigenvalue calibration method (MECM) in our imaging polarimeter to calibrate not only the PSG and PSA, but also the objective lens, the condenser lens, and mirrors et al. MECM is based on the measurements of a set of reference samples between generalized PSG and PSA including air, a linear polarizer oriented at 0° and 90°, and quarter-wave plate oriented at 30°. After calibration, the Mueller matrices containing the depolarization, diattenuation and retardance properties, as well as the polarization aberration of the polarization elements and weak polarization elements in our system can be obtained. The mean values of each Mueller matrix element of the air after calibration are given in Eq. (1). The measurement errors are less than 0.2%. The detailed calibration process can be found in our previous publication [35].

$$
\bar{\mathbf{M}}_a = \begin{bmatrix} 1 & -0.0006 & -0.0007 & -0.0003 \\ 0.0005 & 1.0000 & 0.0003 & 0.0002 \\ 0.0001 & 0.0000 & 0.9981 & -0.0002 \\ -0.0004 & -0.0001 & -0.0006 & 1.0000 \end{bmatrix}. \tag{1}
$$

2.2. *Mueller matrix polar decomposition*

Mueller matrix is a comprehensive description of the polarization characteristics of the samples. However, the individual Mueller matrix elements often lack explicit connections to the certain characteristic tissue microstructures, so the Mueller matrix decomposition is needed. At present, the main methods of Mueller matrix decomposition for tissue detection is Mueller matrix polar decomposition (MMPD) proposed by Lu and Chipman [38], which can transform the

undefined Mueller matrix elements into polarization parameters with clear significance. The MMPD parameters depolarization (Δ) and retardation (R) can be derived by the Eqs. (2), (3) and (4). In Eq. (2)M_Δ, M_R, M_D are the sub-matrix of depolarization, retardance and diattenuation respectively.

$$M = M_\Delta M_R M_D \tag{2}$$

$$\Delta = 1 - \frac{|tr(M_\Delta - 1)|}{3} \tag{3}$$

$$R = \cos^{-1}\left[\frac{|tr(M_R)|}{2} - 1\right] \tag{4}$$

2.3.   *Otsu's algorithm for image segmentation and gray level co-occurrence matrix for image texture analysis*

Otsu's algorithm is an image segmentation method that maximizes the inter-class variance between the object and background in accordance with the image grayscale characteristics to obtain an optimal segmentation threshold [37]. Assuming that T is the segmentation threshold of object and background in images. The proportion of object pixels to the whole image is ω_0 and the corresponding average gray value is μ_0. The proportion of background pixels to the whole image pixels is ω_1, and the corresponding average gray value is μ_1. The average gray level of the whole image is $\mu = \omega_0 \cdot \mu_0 + \omega_1 \cdot \mu_1$.Then, the inter-class variance of the two regions can be obtained: $g = \omega_0 \cdot (\mu_0 - \mu)^2 + \omega_1 \cdot (\mu_1 - \mu)^2$. Note that inter-class variance g varies with the segmentation threshold T. When the g reaches the maximum, the difference between the object and background will be the largest. At this time, the corresponding T is the best segmentation threshold. The region of object corresponds to the locations where the pixel value is less than T, and the rest region is the background.

The gray level co-occurrence matrix (GLCM) method is widely used for image texture analysis. The GLCM refers to a matrix that is defined over an image to be the distribution of co-occurring pixel greyscale values at a given offset [39,40]. The features of GLCM can be expressed by some scalars: 1) contrast (Ct), which reflects the contrast of the brightness between a pixel and its neighbor; 2) correlation (Cr) that reflects the consistency of image texture; 3) the energy (Er) which characterizes the uniformity and roughness of the image; 4) homogeneity, which reflects the local variation of image texture. The equations for calculating these parameters can be found in [41].

2.4.   *Samples preparation*

In this work, the kidney, bone marrow, blood, muscle, lung and skin tissues of rats were selected to prepare 4μm sections respectively. At the same time, a 4μm low differentiation lung cancer section of human was also prepared, which contains three regions: normal, inflamed, and malignant. Both rat tissue sections and the lung cancer section were formalin-fixed, paraffin-embedded unstained tissue sections. The sections were not dewaxed and kept in paraffin before the polarization measurements. After being measured by the proposed method, the sections were H-E stained (hematoxylin and eosin stained) for further comparative study. The slices used in this paper were all provided by Beijing Zhongke Wanbang Biotechnology Co., Ltd.

3.   **Results and discussion**

3.1.   *Illustration of cellular-level Mueller matrix imaging method with rat tissue sections*

Twelve locations were selected in each tissue section of rat for measurement, one of which was shown to illustrate the implementation process of the cellular-level Mueller matrix imaging method. Figures 2(a0)–(f0) show the microscopic intensity images of the unstained sections

under 100x objective lens with a numerical aperture (NA) of 0.8. Figures 2(a1)–(f1) show the microscopic images of the sections at the same position after staining. The size of imaging area is 600×600 pixels. It can be seen that compared with the stained microscopic images, the microscopic intensity images of the unstained sections are difficult to reflect the microstructure characteristics of the tissues. Then, the Mueller imaging polarimeter was used to measure the selected locations of the unstained sections with the same objective lens. The obtained Mueller matrix was further processed by polar decomposition. Figures 3(a)–(f) show the depolarization images of the unstained sections of different rat tissues. Since the measured section inherently contained paraffin and did not undergo staining, the obtained polarization images were obscured by the polarization information of the paraffin contained in the section. Therefore, it was necessary to identify the distribution of paraffin and remove its effect from the resulting polarization images to obtain the real cellular-level polarization information.

Paraffin crystals display significant birefringent behavior [42]. Therefore, their distribution in the unstained section can be determined by measuring the retardance to eliminate their effects on the resulting polarization images. Figures 4(a)–(f) show the retardance images of the unstained sections of different rat tissues. For lung, blood and bone marrow, which are mainly composed of cells, the area with large retardance mainly corresponds to the intercellular space of the cells. For muscle, skin and kidney, which are composed of cells and collagen fibers, the area with large retardance mainly corresponds to the gap between the tissues. Note that paraffin not only can replace the intercellular tissue fluid but also may enter the interior of cells and form bonds with some components of the nucleus during the section preparation process [43,44]. Many biological tissue types also represent a certain degree of birefringence like muscles. In order to accurately segment the tissue areas, we adopted the Otsu's algorithm. Table 1 shows the distribution range of retardance in tissue areas and gap areas filled with paraffin, and the segmentation thresholds of retardance images calculated by Otsu's algorithm. The process of obtaining the distribution range of retardance values is as follow: Firstly, by comparing with the corresponding stained microscopic images, the locations of the tissue areas and gap areas in the retardance images are determined. Then 10000 pixels are randomly selected in the two areas respectively for data analysis. Finally, determining the distribution range of pixel values. It can be seen from Table 1 that the gap areas filled with paraffin reflect a much greater retardance than the tissue areas. The thresholds can clearly segment the tissue areas and gap areas, which not affect the integrity of the tissue even containing some cells that may contain paraffin or some structures with birefringence. Figure 5 shows the result of binary retardance images with thresholds, wherein the pixel value in the paraffin region is set to zero (black area).

Table 1. The segmentation thresholds of retardance images calculated by Otsu's algorithm, the distribution range of retardance values in the tissue areas and gap areas

Tissue types	Thresholds (rad)	Tissues areas (rad)	Gap areas (rad)
Kidney	0.5108	0.0115-0.3521	0.5816-1.3207
Bone Marrow	0.2157	0.0186-0.1843	0.3501-0.9528
Blood	0.2863	0.0076-0.2016	0.3734-1.0802
Muscle	0.3118	0.0091-0.2741	0.3313-0.9957
Lung	0.3765	0.0125-0.2122	0.4157-1.7635
Skin	0.5804	0.0300-0.3495	0.5965-3.1251

After removing the effects of paraffin, the depolarization images were obtained by setting the depolarization value of the gap areas filled with paraffin to zero. The obtained images were compared with the corresponding microscopic images after section staining. An appropriate color bar was selected for improved illustration, as shown in Fig. 6. It is observed that good agreement exists between the depolarization images after paraffin effect removal and the stained
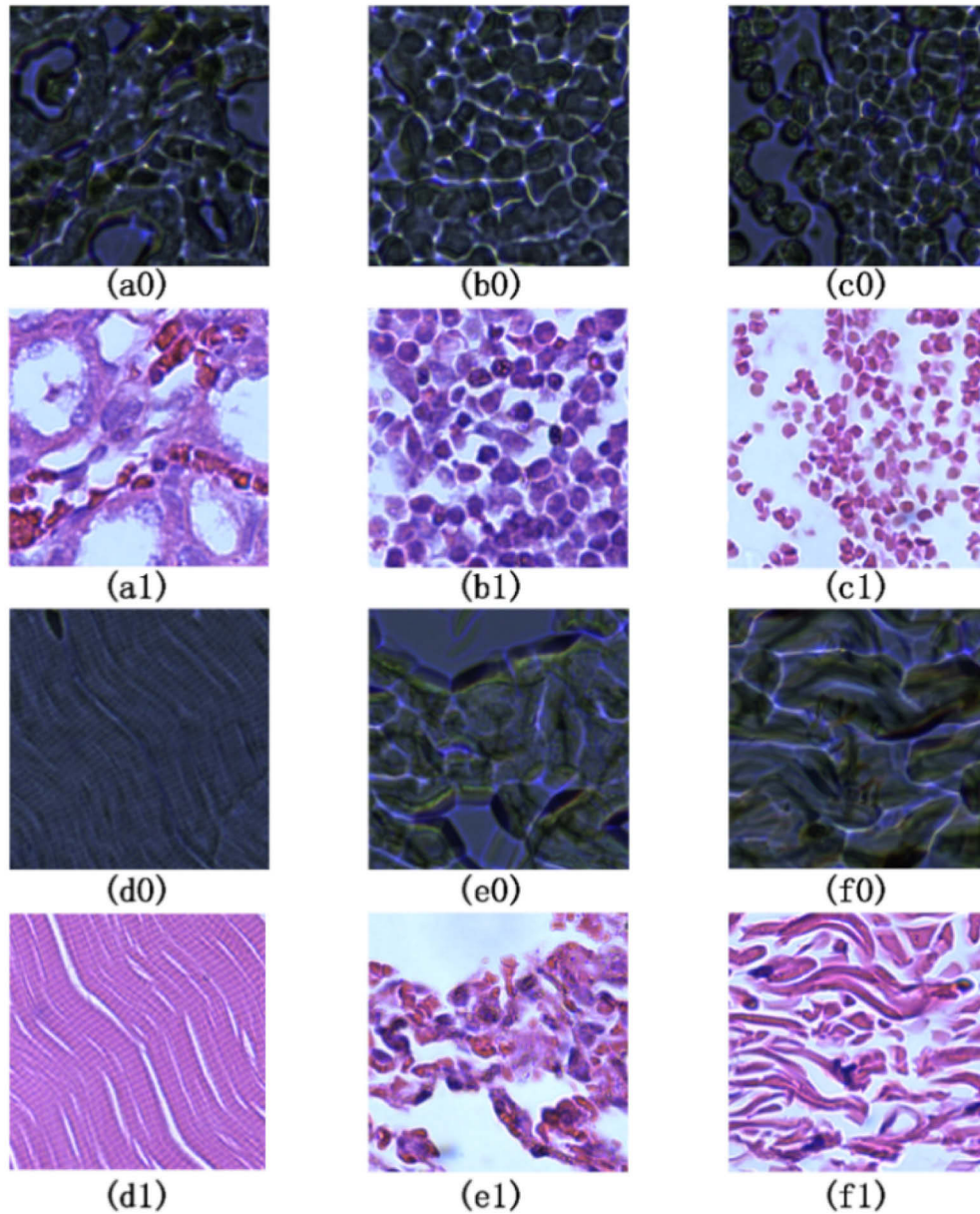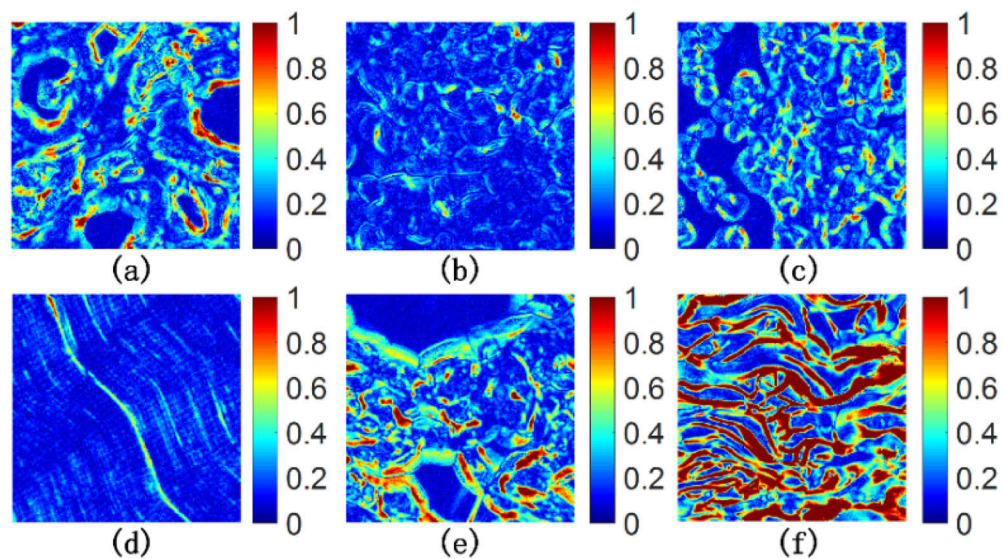
Fig. 2. (a0)–(f0) the microscopic intensity images of the unstained sections. (a1)–(f1) corresponding microscopic images of (a0)–(f0) after section staining. (a0), (a1) kidney; (b0), (b1) bone marrow; (c0), (c1) blood; (d0), (d1) muscle; (e0), (e1) lung; (f0), (f1) skin.
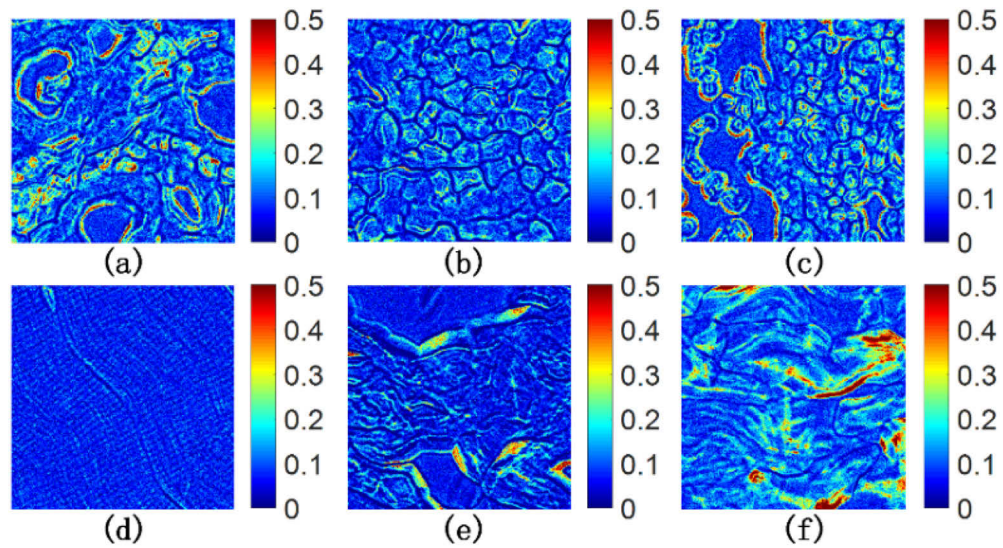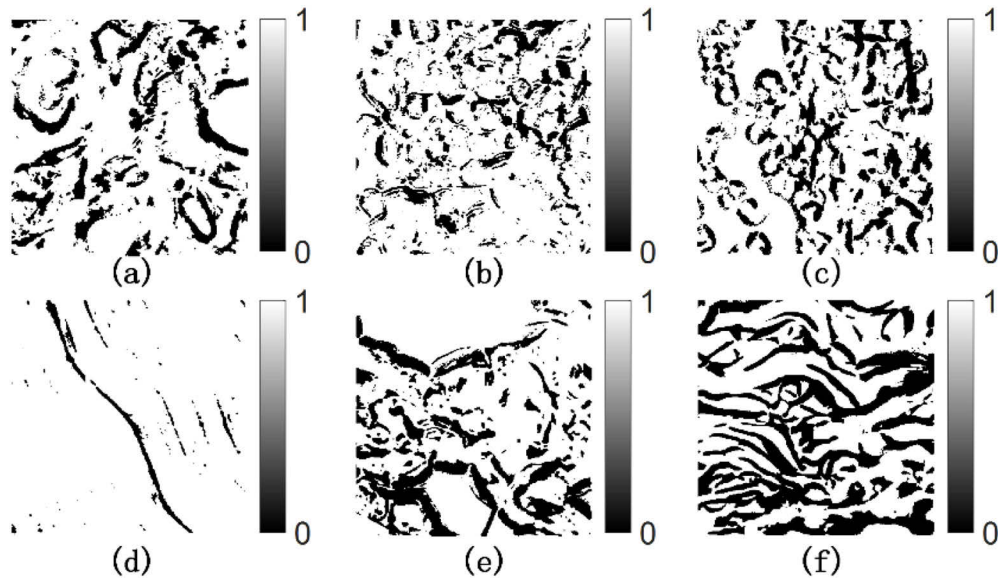
Fig. 3. Depolarization images of the unstained sections of different rat tissues: (a) kidney; (b) bone marrow; (c) blood; (d) muscle; (e) lung; (f) skin.

Fig. 4. Retardance images of the unstained sections of different rat tissues: (a) kidney; (b) bone marrow; (c) blood; (d) muscle; (e) lung; (f) skin.

Fig. 5. Binary retardance images of the unstained sections of different rat tissues: (a) kidney; (b) bone marrow; (c) blood; (d) muscle; (e) lung; (f) skin.

microscopic images. Here, a quantitative description is provided on the similarity between the stained microscopic images and the depolarization images before and after the paraffin effect is removed. Owing to the non-simultaneous measurement of the depolarization images and the stained microscopic images, some overlay would have been generated when the slice was placed, resulting in the inability to compare the similarity between two images, pixel by pixel. Therefore, the following process was adopted to quantitatively evaluate the similarity between the two images. We first analyzed the image texture using the gray level co-occurrence matrix method. We extracted the contrast, correlation, energy, and homogeneity of each image to form a column vector, which was used as the image texture-feature vector. Then, the correlation coefficients between the texture-feature vectors of the depolarization images and stained microscopic images were compared. A greater similarity was evident between the two images having a larger correlation coefficient. Compared with the depolarization images that had the paraffin effect, the depolarization images without the paraffin effect showed a significantly higher similarity with the stained microscopic images (average correlation coefficient greater than 0.8), as shown in Table 2, which more realistically reflected the morphology and arrangement of the cells. In the table, the correlation coefficient of each tissue sample is the average of the 12 measured locations. Due to the morphology of the cells changed slightly after the section was immersed in chemical agents during the staining process, a slight gap still occurred between the calculated correlation coefficient and 1. At the same time, the polarization images without the influence of paraffin reflected the real polarization information of the tissues at the cellular level. Table 3 quantitatively reflects the mean and standard deviation of the depolarization in 12 imaging areas of each tissue.

3.2. Polarization measurement of the lung cancer slice of human by using the cellular-level Mueller matrix imaging method

Using the above method, we respectively selected 10 locations for normal, inflamed and malignant areas in the unstained sections of human lung cancer for polarization measurement. Figure 7 shows the depolarization images of two of them after removing the influence of paraffin and the
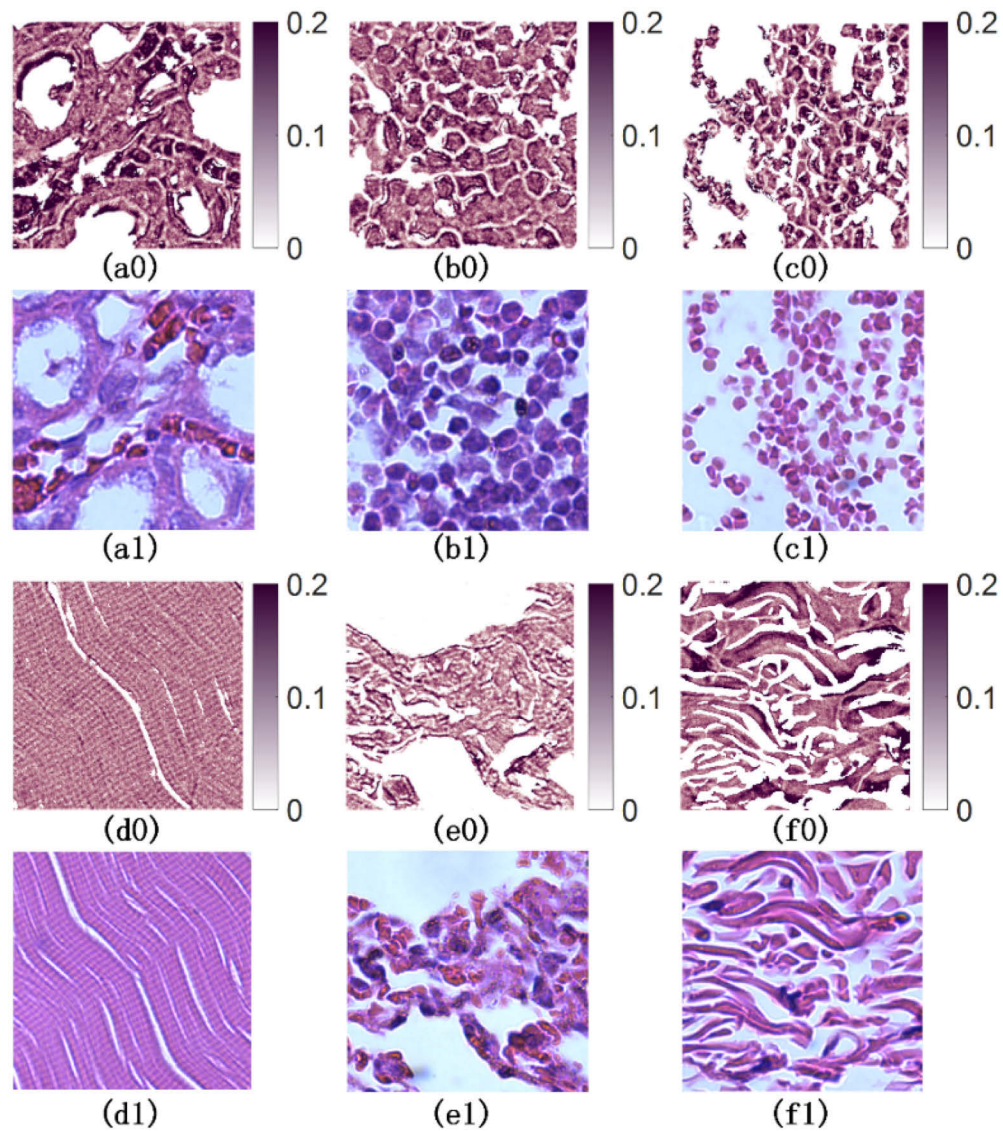
Fig. 6. (a0)–(f0) the depolarization images after removing the paraffin effects. (a1)–(f1) corresponding microscopic images after section staining. (a0), (a1) kidney; (b0), (b1) bone marrow; (c0), (c1) blood; (d0), (d1) muscle; (e0), (e1) lung; (f0), (f1) skin.

Table 2. Statistical analysis of correlation coefficients of the feature texture vectors of the depolarization images and the stained microscopic images

Region (n = 12)	With paraffin effect		Without paraffin effect	
	Mean	SD	Mean	SD
Kidney	0.5007	0.2151	0.9012	0.0617
Bone Marrow	0.2713	0.1145	0.8663	0.1143
Blood	0.6510	0.2639	0.8422	0.4164
Muscle	0.4842	0.1803	0.8744	0.1576
Lung	0.3734	0.1380	0.8552	0.1550
Skin	0.4011	0.1170	0.8026	0.1211

Table 3. Statistical analysis of depolarization parameters without paraffin effect for different tissue samples

Region (n = 12)		Kidney	Bone Marrow	Blood	Muscle	Lung	Skin
The entire images of the depolarization ($\Delta\times10^4$)	Mean	2.9970	2.5035	1.2316	2.1608	1.6235	2.4423
	SD	0.1119	0.1018	0.8271	0.2279	0.1334	0.0905

corresponding stained microscopic images. Table 4 quantitatively shows the similarity between the stained microscopic images and the depolarization images before and after the paraffin effect is removed. It can be seen that the depolarization images without paraffin effect show greater agreement with that of traditional stained microscopic images in term of the morphology and arrangement of the cells, realizing the accurate identification of different areas (normal, inflamed, and malignant) on the unstained slice. Besides the depolarization images obtained after eliminating the paraffin influence also provided the real cellular-level depolarization information of tissue. Table 5 shows the quantitative statistical results of the depolarization characteristics of normal, inflamed and malignant areas in the sections. It can be seen that the depolarization value of malignant areas is higher than that of normal areas and inflamed areas, whether it is the whole image or single cell. The depolarization value of cells in inflamed region was the smallest, and that of cells in normal region was in the middle. Therefore, depolarization parameters have the potential to be a standard for distinguishing different types of cells in lung cancer sections.

Table 4. Statistical analysis of correlation coefficients of the feature texture vectors of the depolarization images and the stained microscopic images

Region (n = 10)	With paraffin effect		Without paraffin effect	
	Mean	SD	Mean	SD
normal	0.4515	0.3277	0.8367	0.1705
inflamed	0.5530	0.2137	0.8061	0.2977
malignant	0.2701	0.2424	0.8006	0.1830

Table 5. Statistical analysis of depolarization parameters without paraffin effect for the normal inflamed and malignant areas of the lung cancer section

Region (n = 10)	The range of cell number of the imaging areas	The entire images of the depolarization (Δ) (10^4)		The single cell of the depolarization ($\Delta\times10^4$)	
		Mean	SD	Mean	SD
normal	33~45	1.7851	0.2941	0.0443	0.0043
inflamed	104~117	2.6298	0.1725	0.0238	0.0019
malignant	50~59	2.7519	0.1471	0.0505	0.0038

From the depolarization images, we can also analyze the structural information within the cells. Depolarization is mainly caused by the scattering of light inside the tissue. For cells in normal regions, scattering occurs as a consequence of microstructures formed by a large number of organelles and chromatin. In contrast, the interior of malignant cells is almost occupied by the nucleus, and the chromatin within the nucleus contributes to the primary scattering of light. The lymphocytes and neutrophils in the inflamed tissue also demonstrate a large ratio of the nucleus to cytoplasm, showing a similar light scattering pattern to that of malignant tissue. It is worth noting that the depolarization values contributed by different cells in a single image are not equal. In inflamed tissue, the inflammation symptom is often complicated by bleeding. Therefore, many red blood cells are present in the tissue along with the lymphocytes and neutrophils. Because
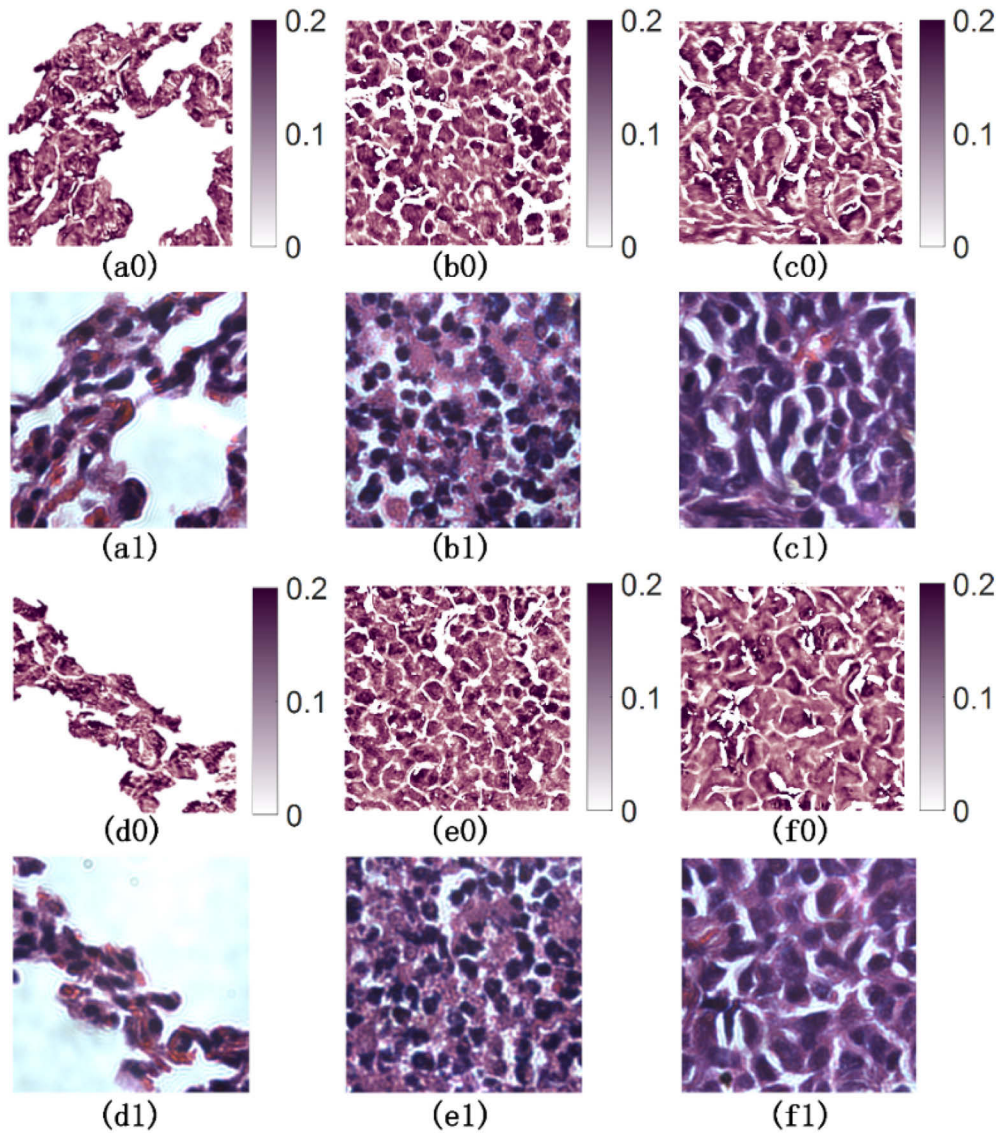
Fig. 7. (a0)–(f0) depolarization images after removing the paraffin effects. (a1)–(f1) corresponding microscopic images after section staining. (a0), (a1) and (d0), (d1) normal; (b0), (b1) and (e0), (e1) inflamed; (c0), (c1) and (f0), (f1) malignant.

red blood cells have no nuclei, the amount of light scattering is smaller, thus yielding weaker depolarization. In cancer tissue, the degree of differentiation and the concentration of chromatin in the nucleus vary for different malignant cells, leading to depolarization differences. Therefore, depolarization may serve as a criterion for identifying the cell type in inflamed tissue and for assessing the degree of differentiation of malignant cells.

4.   Conclusion

In this study, a cellular-level Mueller matrix imaging method of unstained sections was proposed for the first time. In this method, the polarization images at the cellular level are first obtained by Mueller matrix measurement. Then, for the retardance images, Otsu's algorithm is employed to locate the region where paraffin is distributed. Finally, the paraffin effects are removed from the depolarization images to obtain the polarization information of only the tissues. The proposed method can not only obtain the real cellular-level polarization information of tissue but also can exactly identify the cell structure in the unstained sections. This method also has the advantages of not requiring time-consuming staining and eliminating the risk of misdiagnosis caused by poor staining. In this paper, we illustrate the detailed implementation process of the cellular-level Mueller matrix imaging method by measuring different tissue sections of rats, and quantitatively prove the accuracy of the depolarization images obtained by this method to reflect the morphology and arrangement of the tissue in unstained sections at the cellular level. Subsequently, the proposed method was applied to measure human lung cancer tissue section and accurately realized the identification of normal inflamed and malignant areas in the unstained section. Quantitative analysis showed that the cells in different areas of lung cancer section showed different size of depolarization value: the cancer cells were the largest, the inflamed cells were the smallest, and the normal cells were in the middle, which has the potential to be a standard for distinguishing different types of cells in lung cancer sections. The method proposed in this paper paves a possible way for the rapid and accurate diagnosis of cancer in the future.

Disclosures. The authors declare that there are no conflicts of interest related to this article.

Data availability. Data underlying the results presented in this paper are not publicly available at this time but may be obtained from the authors upon reasonable request.

References

1. C. A. Seldenrijk, B. C. Morson, S. G. Meuwissen, N. W. Schipper, J. Lindeman, and C. J. Meijer, "Histopathological evaluation of colonic mucosal biopsy specimens in chronic inflammatory bowel disease: diagnostic implications," Gut **32**(12), 1514–1520 (1991).
2. C. Thomas and King, *Integrated Pathology* (Academic, 2014) Chap. 5.
3. C. R. Drifka, A. G. Loeffler, K. Mathewson, G. Mehta, A. Keikhosravi, Y. Liu, S. Lemancik, W. A. Ricke, S. M. Weber, and W. J. Kao, "Comparison of picrosirius red staining with second harmonic generation imaging for the quantification of clinically relevant collagen fiber features in histopathology samples," J Histochem Cytochem. **64**(9), 519–529 (2016).
4. T. Okimura, Z. Jiang, H. Komatsubara, K. Hirasaka, and T. Oda, "Therapeutic effects of an orally administered edible seaweed-derived polysaccharide preparation, ascophyllan HS, on a Streptococcus pneumoniae infection mouse model," International Journal of Biological Macromolecules **154**, 1116–1122 (2020).
5. D. Bancroft and S. K. Suvarna, *Theroy and Practice of Histological Techniques*, 8th ed. (Academic, 2019).
6. B. Saikia, K. Gupta, and U. N. Saikia, "The modern histopathologist: in the changing face of time," Diagn. Pathol. **3**(1), 25–29 (2008).
7. R. Horobin and J. Kiernan, *Conn's Biological Stains: A Handbook of Dyes, Stains and Fluorochromes for Use in Biology and Medicine* (BIOS Scientific Publishers, 2002).
8. . BjRn, and A. Afzelius, "Section staining for electron microscopy using tannic acid as a mordant: A simple method for visualization of glycogen and collagen," Microsc. Res. Tech. **21**(1), 65–72 (1992).
9. S. Alali and I. A. Vitkin, "Polarized light imaging in biomedicine: Emerging Mueller matrix methodologies for bulk tissue assessment," J. Biomed. Opt. **20**(6), 061104 (2015).

10. B. Jones, G. Thomas, J. Westreich, S. Nofech-Mozes, A. Vitkin, and M. Khorasani, "Novel quantitative signature of tumor stromal architecture: polarized light imaging differentiates between myxoid and sclerotic human breast cancer stroma," Biomed. Opt. Express **11**(6), 3246–3262 (2020).

11. N. Ghosh and I. A. Vitkin, "Tissue polarimetry: Concepts, challenges, applications, and outlook," J. Biomed. Opt. **16**(11), 110801 (2011).

12. V. V. Tuchin, "Polarized light interaction with tissues," J. Biomed. Opt. **21**(7), 071114 (2016).

13. J. Qi and D. S. Elson, "Mueller polarimetric imaging for surgical and diagnostic applications: A review," J. Biophotonics **10**(8), 950–982 (2017).

14. H. He, R. Liao, N. Zeng, P. Li, and H. Ma, "Mueller Matrix Polarimetry—An Emerging New Tool for Characterizing the Microstructural Feature of Complex Biological Specimen," J. Lightwave Technol. **37**(11), 2534–2548 (2019).

15. M. Dubreuil, F. Tissier, S. Rivet, and Y. L. Grand, "Linear diattenuation imaging of biological tissues with near infrared Mueller scanning microscopy," Biomed. Opt. Express **12**(1), 41–54 (2021).

16. R. M. A. Azzam, "Propagation of partially polarized light through anisotropic media with or without depolarization: A differerntial 4 × 4 matrix calculus," J. Opt. Soc. Amer. **68**(12), 1756–1767 (1978).

17. N. O. Quijano and J. L. ArceDiego, "Depolarizing differential Mueller matrices," Opt. Lett. **36**(13), 2429–2431 (2011).

18. N. O. Quijano and J. L. ArceDiego, "Mueller matrix differential decomposition," Opt. Lett. **36**(10), 1942–1944 (2011).

19. S. Kumar, H. Purwar, R. Ossikovski, I. A. Vitkin, and N. Ghosh, "Comparative study of differential matrix and extended polar decomposition formalisms for polarimetric characterization of complex tissue-like turbid media," J. Biomed. Opt. **17**(10), 105006 (2012).

20. R. Ossikovski, "Differential and product Mueller matrix decompositions: a formal comparison," Opt. Lett. **37**(2), 220–222 (2012).

21. R. Ossikovski, "Retrieval of a nondepolarizing estimate from an experimental Mueller matrix through virtual experiment," Opt. Lett. **37**(4), 578–580 (2012).

22. P. Shukla and A. Pradhan, "Mueller decomposition images for cervical tissue: potential for discriminating normal and dysplastic states," Opt. Express **17**(3), 1600–1609 (2009).

23. C. He, H. He, J. Chang, D. Yang, S. Liu, N. Zeng, Y. He, and H. Ma, "Characterizing microstructures of cancerous tissues using multispectral transformed Mueller matrix polarization parameters," Biomed. Opt. Express **6**(8), 2934 (2015).

24. M. Sun, H. He, N. Zeng, E. Du, Y. Guo, S. Liu, J. Wu, Y. He, and H. Ma, "Characterizing the microstructures of biological tissues using Mueller matrix and transformed polarization parameters," Biomed. Opt. Express **5**(12), 4223–4234 (2014).

25. A. Pierangelo, A. Nazac, A. Benali, P. Validire, H. Cohen, T. Novikova, B.H. Ibrahim, S. Manhas, C. Fallet, and M. R. Antonelli, "Polarimetric imaging of uterine cervix: a case study," Opt. Express **21**(12), 14120–14130 (2013).

26. Y. Dong, J. Qi, H. He, C. He, S. Liu, J. Wu, D. S. Elson, and H. Ma, "Quantitatively characterizing the microstructural features of breast ductal carcinoma tissues in different progression stages by Mueller matrix microscope," Biomed. Opt. Express **8**(8), 3643 (2017).

27. B. Liu, Y. Yao, R. Liu, H. Ma, and L. Ma, "Mueller polarimetric imaging for characterizing the collagen microstructures of breast cancer tissues in different genotypes," Opt. Commun. **433**, 60–67 (2019).

28. E. Du, H. He, N. Zeng, M. Sun, Y. Guo, J. Wu, S. Liu, and H. Ma, "Mueller matrix polarimetry for differentiating characteristic features of cancerous tissues," J. Biomed. Opt. **19**(7), 076013 (2014).

29. S. L. Jacques, R. Samantham, S. Isenhath, and K. Lee, "Polarized light camera to guide surgical excision of skin cancers," Proc. SPIE **6842**, 1–7 (2008).

30. A. N. Yaroslavsky, V. Neel, and R. R. Anderson, "Fluorescence polarization imaging for delineating nonmelanoma skin cancers," Opt. Lett. **29**(17), 2010–2012 (2004).

31. Y. Wang, H. He, J. Chang, C. He, S. Liu, M. Li, N. Zeng, J. Wu, and H. Ma, "Mueller matrix microscope: a quantitative tool to facilitate detections and fibrosis scorings of liver cirrhosis and cancer tissues," J. Biomed. Opt. **21**(7), 071112 (2016).

32. M. Dubreuil, P. Babilotte, L. Martin, D. Sevrain, S. Rivet, Y. L. Grand, G. L. Brun, B. Turlin, and B. L. Jeune, "Mueller matrix polarimetry for improved liver fibrosis diagnosis," Opt. Lett. **37**(6), 1061–1063 (2012).

33. H. R. Lee, P. Li, C. Lotz, F. K. Groeber-Becker, S. Dembski, E. Garcia-Caurel, R. Ossikovski, H. Ma, and T. Novikova, "Digital histology with Mueller microscopy: how to mitigate an impact of tissue cut thickness fluctuations," J. Biomed. Opt. **24**(7), 076004 (2019).

34. T. Liu, T. Sun, H. He, S. Liu, Y. Dong, J. Wu, and H. Ma, "Comparative study of the imaging contrasts of Mueller matrix derived parameters between transmission and backscattering polarimetry," Biomed. Opt. Express **9**(9), 4413–4428 (2018).

35. J. Li, Y. Li, K. Liu, G. Zhou, L. Liu, and M. Zheng, "Hybrid calibration method of a wide-view-angle Mueller polarimeter for hyper-numerical-aperture imaging systems," Chin. Opt. Lett. **18**(8), 08 (2020).

36. J. H. Li, "Research on Calibration Techniques of High-precision Imaging polarimeters," Ph.D. thesis, University of Beijing Institute of Technology of China (2020).

37. N. Otsu, "A threshold selection method from gray-histogram," IEEE Trans. Syst., Man, Cybern. **9**(1), 62–66 (1979).

38. S. Y. Lu and R. A. Chipman, "Interpretation of Mueller matrices based on polar decomposition," J. Opt. Soc. Am. A **13**(5), 1106–1113 (1996).

39. R. M. Haralick, K. Shanmugam, and I. H. Dinstein, "Textural features for image classification," IEEE Trans. Syst., Man, Cybern. **SMC-3**(6), 610–621 (1973).

40. R. M. Haralock and L. G. Shapiro, *Computer and Robot Vision* (Addison-Wesley Longman Publishing Co., Inc., 1991).

41. https://www.mathworks.com/help/images/ref/graycoprops.html

42. M. Freund, R. Csikos, S. Keszthelyi, and G. Mozes, *Paraffin Products: Properties, Technologies, Applications* (Elsevier Scientific, 1982).

43. A. Vitkunaite, A. Laurinaviciene, B. Plancoulaine, A. Rasmusson, R. Levenson, M. Shribak, and A. Laurinavicius, "Intranuclear birefringent inclusions in paraffin sections by polychromatic polarization microscopy," Sci. Rep. **11**(1), 6275 (2021).

44. J. D. Vlachos, "Birefringence and paraffinophilia of cell nuclei," Stain Technology **43**(2), 89–95 (1968).